Aalborg Universitet

Introduction to Force-dependent Kinematics

Theory and Application to Mandible Modeling

Andersen, Michael Skipper; de Zee, Mark; Damsgaard, Michael; Nolte, Daniel; Rasmussen, John

[Link to publication from Aalborg University](#)

Introduction to Force-dependent Kinematics: Theory and Application to Mandible Modeling

Andersen, Michael Skipper[1]

2   Department of Mechanical and Manufacturing Engineering, Aalborg University
Fibigerstraede 16, DK-9220 Aalborg East, Denmark

4   msa@m-tech.aau.dk

6   **de Zee, Mark**
Department of Health Science and Technology, Aalborg University

8   Fredrik Bajers Vej 7, DK-9220 Aalborg East, Denmark
mdz@hst.aau.dk

10

    Damsgaard, Michael

12   AnyBody Technology A/S
Niels Jernes Vej 10, DK-9220 Aalborg East, Denmark

14   md@anybodytech.com

16   **Nolte, Daniel**
Department of Bioengineering, Imperial College London

18   London, SW7 2AZ, United Kingdom
d.nolte@imperial.ac.uk

20

    Rasmussen, John

22   Department of Mechanical and Manufacturing Engineering, Aalborg University
Fibigerstraede 16, DK-9220 Aalborg East, Denmark

24   jr@m-tech.aau.dk

26

ABSTRACT

28

Knowledge of the muscle, ligament and joint forces is important when planning orthopedic surgeries. Since

30   *these quantities cannot be measured in vivo under normal circumstances, the best alternative is to*

---

[1] Corresponding author, msa@m-tech.aau.dk.

estimate them using musculoskeletal models. These models typically assume idealized joints, which are

32   *sufficient for general investigations but insufficient if the joint in focus is far from an idealized joint. The*

purpose of this study was to provide the mathematical details of a novel musculoskeletal modelling

34   *approach, called Force-dependent Kinematics (FDK), capable of simultaneously computing muscle,*

ligament and joint forces as well as internal joint displacements governed by contact surfaces and

36   *ligament structures.*

The method was implemented into the AnyBody Modeling System and used to develop a subject-specific

38   *mandible model, which was compared to a point-on-plane (POP) model and validated against joint*

kinematics measured with a custom-built brace during unloaded emulated chewing, open and close and

40   *protrusion. Generally, both joint models estimated the joint kinematics well with the POP model*

performing slightly better (Root-Mean-Square Difference (RMSD) of less than 0.75 mm for the POP model

42   *and 1.7 mm for the FDK model). However, substantial differences were observed when comparing the*

estimated joint forces (RMSD up to 24.7 N), demonstrating the dependency on the joint model. Although

44   *the presented mandible model still contains room for improvements, this study shows the capabilities of*

the FDK methodology for creating joint models that take the geometry and joint elasticity into account.

46

INTRODUCTION

Musculoskeletal models are frequently used to gain insight into the muscle, joint

and ligament forces that are otherwise difficult or impossible to measure *in vivo*.

Research into such models has increased over the past decades and they have been

applied in multiple areas, including orthopedics [1], ergonomics [2] and occupational

health [3].

Several musculoskeletal analysis methods exist but the most commonly applied are inverse dynamics [4,5], forward dynamics-based tracking methods [6], electromyography (EMG)-driven models [7] and dynamic optimization [8]. For a thorough review of computational methods, please see Erdemir et al. [9]. Common to these methods is the modeling of joints as idealized kinematic constraints, e.g. the temporamandibular joint (TMJ) as a point-on-a-plane [10] (POP), the intervertebral joints as spherical joints [11], the knee as a revolute [12] and the ankle and subtalar joints as two non-orthogonal revolute joints [12]. However, several anatomical and prosthetic joints are non-conforming to such an extent that the forces significantly influence the joint kinematics and the joint's internal force equilibrium. Additionally, joints such as knee and shoulder have complicated geometries that are difficult to model accurately using idealized joint models. In such joints, the joint kinematics is governed by an interaction between the muscle actions, contact mechanics and ligaments. Direct measurement of these movements is also difficult with the methods available in most clinics because the movements are small compared to the principal articulations and obscured by the surrounding soft tissue [13].

A few studies have previously incorporated detailed joint models in musculoskeletal models [14-16]. Thelen et al. [14] extended Computed Muscle Control (CMC) [6] to co-simulate detailed musculoskeletal dynamics and knee joint mechanics. This method utilizes feed forward and feedback control to track measured movements and assumes that the joint translation accelerations are instantaneously zero. Halloran et al. [15] used a dynamic optimization problem to predict muscle excitations that

minimize a given performance criterion and included a Finite Element (FE) foot model. They reported computation times of over 10 days. Lei and Fregly [16] introduced a two-level optimization approach to incorporate an elastic foundation-based contact knee model into a musculoskeletal model. In their formulation, the outer optimization searched for the muscle activations that minimized the chosen muscle recruitment criterion while the inner optimization searched for the femoral position such that static equilibrium between all applied loads, muscle and contact forces was obtained. Both optimization problems were solved using non-linear least-squares minimization. However, the frequently used muscle recruitment criteria, e.g. polynomial [4], min/max [5], or energy-based criteria [17], are convex optimization problems for which specialized, efficient and robust algorithms have been developed [18]. By handling muscle recruitment in the outer loop, the approach of Lei and Fregly [16] does not allow the use of optimization solvers tailored to these muscle recruitment criteria.

Andersen et al. [19] introduced the Force-dependent Kinematics (FDK) method, which has been implemented into the AnyBody Modeling System (AMS) and subsequently applied by several, independent research groups to study, among others, knees [20], hips [21], shoulders [22] and spine [23]. The FDK methodology augments an inverse dynamic analysis method with the possibility of not only computing muscle and joint reaction forces but also joint kinematics, taking into account complex joint geometry and elasticity of the surrounding soft tissues. While the abstract by Andersen et al. [19] introduced the idea of FDK, the underlying mathematical and mechanical description has not yet been published. Also, the original FDK method assumed a

4

kinematically determinate description of the model movements. However, this approach limits the possibility of combining marker-based motion capture information with a detailed force-based joint description. Therefore, this paper extends our previous abstract [19] to provide a full description of the mathematical and mechanical formulation of FDK including its connection to kinematically determinate and over-determinate motion data. Additionally, we demonstrate the capabilities of the method for developing a subject-specific model exemplified here by a mandible.

MATERIALS AND METHODS

Force-dependent Kinematics

The idea behind FDK is to extend the output of an inverse dynamic analysis to include the movements in some of the degrees of freedom (DOF) in the model. Let the movements of these $n^{\text{(FDK)}}$ DOFs be denoted as $\boldsymbol{\alpha}^{\text{(FDK)}}$, and refer to them as the FDK DOFs. We shall assume that these FDK DOFs experience "small" movements and the dynamics occurring in these DOFs are negligible. We denote the residual forces in the FDK directions $\mathbf{f}^{\text{(FDK)}}$ and introduce as many FDK residual forces as there are FDK DOFs in the model. With these assumptions, an iterative scheme is wrapped around the inverse dynamics analysis that computes the positions in the FDK DOFs such that the forces acting along these DOFs are in static equilibrium for each time step in the simulation, which is accomplished when the FDK residual forces are zero (see Fig. 1). Note, however, that the full dynamics in all other DOFs are taken into account.

To describe the kinematic analysis and muscle recruitment, we adopt the notations and approaches presented by Andersen et al. [24] and Damsgaard et al. [25]. In terms of notation, we denote scalars with lower case normal letters, vectors with lower case bold letters and matrices with bold, upper case letters. All vectors are defined as column vectors. The definition and dimensionality of all variables are presented in the nomenclature list.

Kinematic analysis

The first step of the iterative scheme is to compute the positions, velocities and accelerations of all the involved segments for a given $\boldsymbol{\alpha}^{(\text{FDK})}$ while assuming that $\dot{\boldsymbol{\alpha}}^{(\text{FDK})} = \ddot{\boldsymbol{\alpha}}^{(\text{FDK})} = \mathbf{0}$.

The position and orientation of the ith segment is denoted by $\mathbf{q}_i = \begin{bmatrix} \mathbf{r}_i^{\text{T}} & \mathbf{p}_i^{\text{T}} \end{bmatrix}^{\text{T}}$ where $\mathbf{r}_i$ is the position of the center of mass and $\mathbf{p}_i$ are the Euler parameters describing its orientation. Additionally, the velocity of the ith segment is denoted by $\mathbf{v}_i = \begin{bmatrix} \dot{\mathbf{r}}_i^{\text{T}} & \boldsymbol{\omega}_i^{'\text{T}} \end{bmatrix}^{\text{T}}$, where $\boldsymbol{\omega}_i^{'}$ is the angular velocity of the segment measured relative to its body-fixed reference frame. The positions and velocities of all bodies are assembled in vectors $\mathbf{q} = \begin{bmatrix} \mathbf{q}_1^{\text{T}} & \mathbf{q}_2^{\text{T}} & \dots & \mathbf{q}_n^{\text{T}} \end{bmatrix}^{\text{T}}$ and $\mathbf{v} = \begin{bmatrix} \mathbf{v}_1^{\text{T}} & \mathbf{v}_2^{\text{T}} & \dots & \mathbf{v}_n^{\text{T}} \end{bmatrix}^{\text{T}}$, respectively. Please note that FDK DOFs, the segment positions, orientations and velocities are all functions of time but the arguments have been omitted in the interest of keeping the equations concise. The joints, the movement and the relationship between the segment coordinates and the FDK DOFs are described by means of constraint equations:

6

$$\mathbf{\Phi}(\mathbf{q}, t) = \mathbf{0}$$
$$\mathbf{\Phi}^{(FDK)}(\mathbf{q}) - \mathbf{\alpha}^{(FDK)} = \mathbf{0},$$

(1)

where $\mathbf{\Phi}(\mathbf{q}, t)$ denotes the joints and drivers in the system and $\mathbf{\Phi}^{(FDK)}(\mathbf{q})$ specifies the

FDK DOFs. The interpretation of the latter equations is that $\mathbf{\alpha}^{(FDK)}$ controls the

kinematic quantity observed by $\mathbf{\Phi}^{(FDK)}(\mathbf{q})$. For instance, if elements of $\mathbf{\Phi}^{(FDK)}(\mathbf{q})$

computes a vector between two points on adjoining segments, the corresponding

elements of $\mathbf{\alpha}^{(FDK)}$ specify the values of this vector, i.e. $\mathbf{\Phi}^{(FDK)}(\mathbf{q}) = \mathbf{\alpha}^{(FDK)}$ Similarly,

$\mathbf{\Phi}^{(FDK)}(\mathbf{q})$ can express a joint angle as a function of the segment orientations or any

other geometrical quantity that can be expressed as a function of the segment positions

and orientations. While $\mathbf{\Phi}^{(FDK)}(\mathbf{q})$ could theoretically be an explicit function of time

similar to the other constraints, $\mathbf{\Phi}(\mathbf{q}, t)$, we have not yet found a practical case where

this would be beneficial. The purpose of the $\mathbf{\Phi}^{(FDK)}(\mathbf{q})$ is solely to express the

relationship between the segment positions and orientations and the degree of

freedoms along which it is desired to compute the movement rather than provide it as

input.

Determinate kinematic analysis

If there are as many independent constraint equations as there are unknown

coordinates, i.e. a kinematically determinate set of equations, the equations can be

solved using a numerical method, e.g. the Newton-Raphson method. Subsequently, the

linear velocity equations:

$$\Phi_{\hat{\mathbf{q}}}\mathbf{v} = -\Phi_t$$

$$\Phi_{\hat{\mathbf{q}}}^{(FDK)}\mathbf{v} = \mathbf{0},$$

(2)

and acceleration equations:

$$\Phi_{\hat{\mathbf{q}}}\dot{\mathbf{v}} = \gamma$$

$$\Phi_{\hat{\mathbf{q}}}^{(FDK)}\dot{\mathbf{v}} = \gamma^{(FDK)},$$

(3)

must be solved to obtain the segment velocities and accelerations, respectively, where the assumptions that $\dot{\boldsymbol{\alpha}}^{(FDK)} = \ddot{\boldsymbol{\alpha}}^{(FDK)} = 0$ have been applied. These equations have been derived by differentiation of Eq. (1) with respect to time. $\Phi_{\hat{\mathbf{q}}}$ is the Jacobian matrix of the constraint equations with respect to a virtual set of positions $\hat{\mathbf{q}}$, that correspond to $\mathbf{v}$ (see Damsgaard et al. [25]), Φ_t is the partial derivative of the constraint equations with respect to time and γ and $\gamma^{(FDK)}$ contain the position- and velocity-dependent terms from the differentiation of Eq. (2) with respect to time. Note that $\hat{\mathbf{q}}$ only makes sense as infinitesimal values applied in differentiation but not as finite values [25]. Additionally, note that the arguments for the derivatives of functions are omitted.

Over-determinate kinematic analysis

Commonly, the motions of musculoskeletal models are measured using motion capture technologies. As described by Andersen et al. [24], this usually results in more measured DOFs than the model comprises and the kinematic analysis approach for determinate systems described above cannot be applied. To solve this, Andersen et al. [24] split the equations into two sets: 1) $\Phi(\mathbf{q},t)$ that must always be fulfilled, referred to as "hard" constraints and 2) $\Psi(\mathbf{q},t)$ that has to be solved "as well as possible",

8

referred to as "soft" constraints. With this split, position analysis can be cast as an

optimization problem [24]:

$$
\begin{aligned}
\min_{\mathbf{q}} \quad & G\big(\mathbf{\Psi}(\mathbf{q},t)\big) \\
\text{s.t.} \quad & \mathbf{\Phi}(\mathbf{q},t)=\mathbf{0} \\
& \mathbf{\Phi}^{(\mathrm{FDK})}(\mathbf{q})-\mathbf{\alpha}^{(\mathrm{FDK})}=\mathbf{0},
\end{aligned}
\tag{4}
$$

where $G\big(\mathbf{\Psi}(\mathbf{q},t)\big)$ is a scalar objective function.

Typically, a weighted least-square objective function

$$
G\big(\mathbf{\Psi}(\mathbf{q},t)\big)=\frac{1}{2}\mathbf{\Psi}(\mathbf{q},t)^{T}\mathbf{W}(t)\mathbf{\Psi}(\mathbf{q},t)
\tag{5}
$$

is used to solve this optimization problem. The term $\mathbf{W}(t)$ is a, possibly, time-varying,

weight matrix. Subsequently, velocity and acceleration analysis must be performed. One

approach is to solve the linear set of equations, originating from time-differentiation of

the Karush-Kuhn-Tucker (KKT) conditions for the optimization problem in Eq. (4) [24], for

the unknown velocities and accelerations. Although this approach leads to velocity and

acceleration estimates within machine precision, the method has the drawback that it

requires analytical third-order derivatives which may be difficult to obtain for advanced

kinematic constraint equations. In this study, instead of using analytical derivatives, we

applied a finite-difference-based approach in which the velocities and accelerations of

the system coordinates are approximated. When the optimization problem in Eq (4) has

been solved, it is possible to compute and subtract the residual, $\mathbf{\delta}(t)$, of the soft

constraint equations such that all constraint equations are equal to zero:

$$
\begin{aligned}
\mathbf{\Psi}(\mathbf{q},t)-\mathbf{\delta}(t)&=\mathbf{0} \\
\mathbf{\Phi}(\mathbf{q},t)&=\mathbf{0} \\
\mathbf{\Phi}^{(\mathrm{FDK})}(\mathbf{q})-\mathbf{\alpha}^{(\mathrm{FDK})}&=\mathbf{0}.
\end{aligned}
\tag{6}
$$

By differentiation of this set of equations with respect to time, a linear set of equations with unknown velocities is obtained. However, this set of equations includes the time derivative of the residual vector, which is not generally known analytically. To approximate the derivative of the residual vector, the residual of the soft constraints at Δt before and after the current analysis time step was computed from which the velocity of the residual can be approximated with a central difference:

$$\dot{\boldsymbol{\delta}}_{\text{approx}} = \frac{\boldsymbol{\Psi}(\mathbf{q}(t+\Delta t), t+\Delta t) - \boldsymbol{\Psi}(\mathbf{q}(t-\Delta t), t-\Delta t)}{2\Delta t}. \tag{7}$$

Hereby, the over-determinate velocity equations are written as:

$$\begin{aligned} \boldsymbol{\Psi}_{\hat{\mathbf{q}}}\mathbf{v} + \boldsymbol{\Psi}_t - \dot{\boldsymbol{\delta}}_{\text{approx}} &= \mathbf{0} \\ \boldsymbol{\Phi}_{\hat{\mathbf{q}}}\mathbf{v} + \boldsymbol{\Phi}_t &= \mathbf{0} \\ \boldsymbol{\Phi}_{\hat{\mathbf{q}}}^{(\text{FDK})}\mathbf{v} &= \mathbf{0}. \end{aligned} \tag{8}$$

Since this generally leads to more equations than necessary, we computed the velocities that minimize the least-square error on the approximated velocity equations subject to the hard constraints and the constraint on the FDK DOFs:

$$\begin{aligned} \min_{\mathbf{v}} \quad & \frac{1}{2}\left(\boldsymbol{\Psi}_{\hat{\mathbf{q}}}\mathbf{v} + \boldsymbol{\Psi}_t - \dot{\boldsymbol{\delta}}_{\text{approx}}\right)^T \left(\boldsymbol{\Psi}_{\hat{\mathbf{q}}}\mathbf{v} + \boldsymbol{\Psi}_t - \dot{\boldsymbol{\delta}}_{\text{approx}}\right) \\ \text{s.t.} \quad & \boldsymbol{\Phi}_{\hat{\mathbf{q}}}\mathbf{v} + \boldsymbol{\Phi}_t = \mathbf{0} \\ & \boldsymbol{\Phi}_{\hat{\mathbf{q}}}^{(\text{FDK})}\mathbf{v} = \mathbf{0}. \end{aligned} \tag{9}$$

With a similar approach, an optimization problem to compute the approximate accelerations is set up:

$$\begin{aligned} \min_{\dot{\mathbf{v}}} \quad & \frac{1}{2}\left(\boldsymbol{\Psi}_{\hat{\mathbf{q}}}\dot{\mathbf{v}} - \boldsymbol{\gamma}^{(\boldsymbol{\Psi})} - \ddot{\boldsymbol{\delta}}_{\text{approx}}\right)^T \left(\boldsymbol{\Psi}_{\hat{\mathbf{q}}}\dot{\mathbf{v}} - \boldsymbol{\gamma}^{(\boldsymbol{\Psi})} - \ddot{\boldsymbol{\delta}}_{\text{approx}}\right) \\ \text{s.t.} \quad & \boldsymbol{\Phi}_{\hat{\mathbf{q}}}\mathbf{v} - \boldsymbol{\gamma} = \mathbf{0} \\ & \boldsymbol{\Phi}_{\hat{\mathbf{q}}}^{(\text{FDK})}\ddot{\mathbf{v}} - \boldsymbol{\gamma}^{(\text{FDK})} = \mathbf{0}, \end{aligned} \tag{10}$$

where $\gamma^{(\Psi)}$ contains the position- and velocity-dependent terms of the soft constraint

equations differentiated twice with respect to the time and $\ddot{\delta}_{approx}$ contains the

approximated second derivative of the residual vector.

Muscle recruitment

With the segment positions, velocities and accelerations computed, the muscle

recruitment problem can be set up and solved. Since there are in general more muscles

in the model than there are DOFs and because musculoskeletal models frequently

contain closed kinematic loops, there are not enough dynamic equilibrium equations to

determine the muscle forces uniquely [9]. To solve this, it is common to assume that the

forces in the system are distributed according to some optimality criterion [4,5,9].

Multiple muscle recruitment criteria can be used, but the discussion of the best criterion

is beyond the scope of this manuscript and we instead refer the reader to the review by

Erdemir et al. [9].

Generally, the muscle recruitment problem is formulated as an optimization problem of

the following form [5,25]:

$$
\begin{aligned}
&\min_{\mathbf{f}} && H\!\left(\mathbf{f}^{(M)}\right) \\
&\text{s.t.} && \begin{bmatrix} \mathbf{C}^{(M)} & \mathbf{C}^{(R)} & \mathbf{C}^{(FDK)} \end{bmatrix}
\begin{bmatrix} \mathbf{f}^{(M)} \\ \mathbf{f}^{(R)} \\ \mathbf{f}^{(FDK)} \end{bmatrix} = \mathbf{d} \\
& && \mathbf{0} \le \mathbf{f}^{(M)} \le \mathbf{s},
\end{aligned}
\tag{11}
$$

where $H\!\left(\mathbf{f}^{(M)}\right)$ is the objective function, which is expressed as a function of the muscle

forces, $\mathbf{f}^{(M)}$, $\begin{bmatrix} \mathbf{C}^{(M)} & \mathbf{C}^{(R)} & \mathbf{C}^{(FDK)} \end{bmatrix}$ is the coefficient-matrix for the unknown forces,

11

$\left[\mathbf{f}^{(M)T} \quad \mathbf{f}^{(R)T} \quad \mathbf{f}^{(FDK)T}\right]^{T}$; $\mathbf{f}^{(R)}$ are the joint reaction forces and $\mathbf{d}$ contain all applied loads and inertia forces. The latter inequality states that the muscles can only pull and not generate a force larger than their instantaneous strength, $\mathbf{s}$. The coefficient-matrix associated with the ith segment, we denote: $\left[\mathbf{C}_i^{(M)} \quad \mathbf{C}_i^{(R)} \quad \mathbf{C}_i^{(FDK)}\right]$. The coefficient-matrix associated with the muscle forces, $\mathbf{C}^{(M)}$, is given by the partial derivative of the length between the origin and insertion with respect to $\hat{\mathbf{q}}$:

$\mathbf{C}^{(M)} = \left[{}^1 l_{\hat{\mathbf{q}}}^{(oi)T} \quad {}^2 l_{\hat{\mathbf{q}}}^{(oi)T} \quad \ldots \quad {}^{n^m} l_{\hat{\mathbf{q}}}^{(oi)T}\right]$, where ${}^i l_{\hat{\mathbf{q}}}^{(oi)T}$ is the partial derivative of the origin to insertion length of the ith muscle with respect to $\hat{\mathbf{q}}$ [25]. The coefficient-matrix for the reaction forces is given as the transpose of the partial derivative of $\mathbf{\Phi}(\mathbf{q}, t)$ with respect to $\hat{\mathbf{q}}$ but with the columns associated with pure movement omitted [25]: $\mathbf{C}^{(R)} = \tilde{\mathbf{\Phi}}_{\hat{\mathbf{q}}}^{T}$, where $\tilde{\mathbf{\Phi}}$ denotes the set of constraint equations after the constraints specifying pure movements have been omitted. Similarly, the coefficient-matrix for the FDK residual forces is given as the transpose of the partial derivatives of the FDK constraint equations with respect to $\hat{\mathbf{q}}$: $\mathbf{C}^{(FDK)} = \mathbf{\Phi}_{\hat{\mathbf{q}}}^{(FDK)T}$.

We use the Newton-Euler equations re-organized to fit the form in Eq. (11), which for the ith segment are:

$$\mathbf{C}_i^{(M)}\mathbf{f}^{(M)} + \mathbf{C}_i^{(R)}\mathbf{f}^{(R)} + \mathbf{C}_i^{(FDK)}\mathbf{f}^{(FDK)} = \mathbf{g}_i^{(app)} - \begin{bmatrix} m_i\mathbf{I} & \mathbf{0} \\ \mathbf{0} & \mathbf{J}_i^{'} \end{bmatrix}\dot{\mathbf{v}}_i - \begin{bmatrix} \mathbf{0} \\ \tilde{\mathbf{\omega}}_i^{'}\mathbf{J}_i^{'}\mathbf{\omega}_i^{'} \end{bmatrix}$$

$$\left[\mathbf{C}_i^{(M)} \quad \mathbf{C}_i^{(R)} \quad \mathbf{C}_i^{(FDK)}\right]\begin{bmatrix} \mathbf{f}^{(M)} \\ \mathbf{f}^{(R)} \\ \mathbf{f}^{(FDK)} \end{bmatrix} = \mathbf{d}_i, \tag{12}$$

where m_i is the segment mass, $\mathbf{J}_i'$ is the inertia tensor referring to the body-fixed

frame, $\mathbf{g}_i^{(\mathrm{app})}$ contain the applied loads and:

$$\mathbf{d}_i = \mathbf{g}_i^{(\mathrm{app})} - \begin{bmatrix} m_i \mathbf{I} & \mathbf{0} \\ \mathbf{0} & \mathbf{J}_i' \end{bmatrix} \dot{\mathbf{v}}_i - \begin{bmatrix} \mathbf{0} \\ \tilde{\boldsymbol{\omega}}_i' \mathbf{J}_i' \boldsymbol{\omega}_i' \end{bmatrix}. \tag{13}$$

Hereby, the dynamic equilibrium equations on the required form for Eq. (11) can be

assembled for all the segments:

$$\begin{bmatrix} \mathbf{C}_1^{(\mathrm{M})} & \mathbf{C}_1^{(\mathrm{R})} & \mathbf{C}_1^{(\mathrm{FDK})} \\ \mathbf{C}_2^{(\mathrm{M})} & \mathbf{C}_2^{(\mathrm{R})} & \mathbf{C}_2^{(\mathrm{FDK})} \\ & \vdots & \\ \mathbf{C}_n^{(\mathrm{M})} & \mathbf{C}_n^{(\mathrm{R})} & \mathbf{C}_n^{(\mathrm{FDK})} \end{bmatrix} \begin{bmatrix} \mathbf{f}^{(\mathrm{M})} \\ \mathbf{f}^{(\mathrm{R})} \\ \mathbf{f}^{(\mathrm{FDK})} \end{bmatrix} = \begin{bmatrix} \mathbf{d}_1 \\ \mathbf{d}_2 \\ \vdots \\ \mathbf{d}_n \end{bmatrix}$$

$$\begin{bmatrix} \mathbf{C}^{(\mathrm{M})} & \mathbf{C}^{(\mathrm{R})} & \mathbf{C}^{(\mathrm{FDK})} \end{bmatrix} \begin{bmatrix} \mathbf{f}^{(\mathrm{M})} \\ \mathbf{f}^{(\mathrm{R})} \\ \mathbf{f}^{(\mathrm{FDK})} \end{bmatrix} = \mathbf{d}. \tag{14}$$

With the above formulations of kinematic analysis and the muscle recruitment problem,

it is possible to compute all muscle, joint and FDK residual forces for a given $\boldsymbol{\alpha}^{(\mathrm{FDK})}$.

Hereby, it is possible to systematically search for $\boldsymbol{\alpha}^{(\mathrm{FDK})}$ such that $\mathbf{f}^{(\mathrm{FDK})}$ is zero and in

which case static equilibrium along the FDK DOFs is obtained. Numerically, we apply a

Newton-Raphson-based approach augmented with a golden section line search to

determine $\boldsymbol{\alpha}^{(\mathrm{FDK})}$ such that $\mathbf{f}^{(\mathrm{FDK})}(\boldsymbol{\alpha}^{(\mathrm{FDK})}) = \mathbf{0}$. This approach is illustrated in Fig 1.

Mandible model

To test the method, a subject-specific mandible model was developed. The

mandible offers a unique opportunity of noninvasively obtaining *in vivo* measurements

of the bone movements by attaching a measurement device to the teeth. Therefore, it is an attractive example for this study.

Experimental setup

A cone beam CT scan (NewTom 5G, QR Verona, Italy) of the skull and mandible bones was obtained for one male subject (age 40, mass 70 kg) with an isotropic voxel dimension of 0.3 mm. During the scanning, the teeth were not in an intercuspal position, but separated by two dental cotton rolls, which facilitated the subsequent segmentation. The skull and mandible bones as well as the skin surface were segmented using a visualization software package (Mimics 14.12, Materialise, Leuven, Belgium).

To accurately measure the movement of the mandible relative to the skull, a custom brace was developed (Fig. 2). First, a dental impression of the subject's teeth was obtained by an experienced dentist, after which a dental cast of the subject was created. Second, a 1 mm thick Poly(methyl methacrylate) (PMMA) plastic brace was created to fit over the cast on both the upper and lower part. After hardening the plastic brace, 1.2 mm metal wires were shaped and glued to the outside of the brace, which enabled attaching a 50 x 50 x 6 mm plate made out of Obomodolan 1000 (OBO-Werke GmbH & Co. KG, Stadthagen, Germany). This was accomplished by drilling 1.2 mm holes, in the foam into which the metal wires were inserted together with glue to obtain fixation. At each corner of the Obomodolan plate, 4 mm light weight half-sphere retro-reflective markers (Qualisys, Gothenburg, Sweden) were attached. The total mass of

each of the two braces including the plastic, metal wires, the Obomodolan plates and

markers was approximately 15 g, which we considered negligible in the models.

The project was performed according to the regulations of the local ethical committee.

Motion capture data

To estimate the mandible movements under various tasks, a motion capture

experiment was conducted, where the subject wore the custom brace. All

measurements were performed with the subject seated.

Nine 7-mm light weight, retro-reflective markers were attached to the subject

(see Fig. 2) and their trajectories were tracked using a marker-based motion capture

system, consisting of eight infrared high-speed cameras (Oqus 300 series), sampling at

100 Hz, combined with Qualisys Track Manager v. 2.9 (Qualisys, Gothenburg, Sweden).

The marker placed on the nose as well as the two markers placed on the medial and

lateral sides of the chin where, however, later excluded from the analysis as it turned

out to be difficult to define their location on the segmented skin of the CT scan.

First, a reference trial was collected where the subject occluded his mouth as much as

possible. Subsequently, three dynamic tasks were recorded:

- Task 1: Chewing movement but without producing a bite force, with a frequency

  of approximately 1 Hz.

- Task 2: A cyclic protrusion movement from intercuspal position to sub-maximal

  protrusion corresponding to the incisor-to-incisor position with a frequency of

  approximately 0.5 Hz.

- Task 3: A cycling opening/closing of the mouth to a half-open position.

-

For each task, the subject was instructed to repeat the movements for 10 seconds followed by a small pause. This process was repeated twice for each movement. Subsequently, the first five complete cycles of each movement were extracted for further analysis.

Laser scan of the brace geometries

The brace was laser scanned using a NextEngine Ultra HD 3D scanner (NextEngine, Santa Monica, California) to create a geometrical model. A hole was drilled in the middle of the most posterior edge of each of the casts such that they could be secured to the scanner. Subsequently, the upper and lower parts of the brace were attached to the respective cast and a 360° scan obtained of each part separately.

Musculoskeletal model

The mandible model was developed in the AMS v. 6.0.5 based on the acquired CT scan. A Frankfurt horizontal plane was defined based on the left and right porion and the left orbital. From this, an anatomical reference frame was defined such that the origin was located midway between the most superior point of each condyle of the mandible. The y-axis was constructed by projecting the line connecting the most superior point of the condyles onto the Frankfurt horizontal plane with the axis pointing from right to left. The x-axis was constructed as the line orthogonal to the y-axis

pointing towards the left orbital. The z-axis was computed as the cross product between the x- and y- axis. This reference frame was defined for both the skull and mandible such that the two reference frames were fully aligned in the relative pose of the skull and mandible of the CT scan. The reference frame is depicted in Fig. 2.

To determine the location of the custom-built brace relative to the segmented skull and mandible of the CT scans, the reference trial was used. The locations of the skin markers were identified on the skin surface of the CT scan by the same investigator who placed them during the motion capture session. Similarly, locations of the markers on the brace parts were identified in the laser scan reference frame. Subsequently, a least-squares fit was set up, where the skin markers of the CT scan tracked the measured skin markers and the four markers on each part of the brace tracked the corresponding four markers for the first frame of the reference trial. From this, the relative position and orientation of the laser scan reference frame of each brace part relative to the respective bone reference frame was computed and used to define the four brace markers in the skull and mandible reference frames, respectively (Fig. 2). In all subsequent dynamic trials, the skin markers were not used in the analysis.

Since muscle and ligament insertions were not visible in the CT scan, these were approximated from the bone geometries using the model of de Zee et al. [10] as reference. The model was equipped with 24 Hill-type muscle actuators each consisting of a contractile, serial and parallel elastic element. The mass, inertia and muscle mechanical properties were adapted from de Zee et al. [10], which is based on the peak isometric force and optimum fiber lengths reported by Koolstra and Van Eijden [26].

To model the temporomandibular joints (TMJs), two models of different complexity were developed.

Point-on-plane TMJ model

In the first model, a POP-constrained TMJ model was constructed similarly to de Zee et al. [10]. For each condyle, a single kinematic constraint was introduced to ensure that the most superior point of the condyle was constrained to a plane angled 30° downwards and canted 5° medially relative to the Frankfurt horizontal plane. Since the TMJ is a loose joint, the reaction forces of the joint were constructed such that only compression was allowed. Specifically, this was accomplished by introducing a strong contact element with a constant isometric strength of 20 kN that can only push and its force computed as part of the muscle recruitment (See Eq. (11)). The high strength of this contact element ensures that it behaves like a reaction force (having no cost) in the muscle recruitment optimization. Compared to the isometric strength of the muscles, the strength of the contact element is almost two orders of magnitude larger and it remains activated less than 0.5 % in the simulations, which should make it insignificant in the objective function. Additionally, one constraint equation was introduced that prevented movement along the medial/lateral axis of the skull anatomical reference frame. The model is illustrated in Figure 3.

Kinematic analysis was performed by minimizing the least-squares difference between the eight markers on the brace and the corresponding marker trajectory in the laboratory reference frame using the method of Andersen et al. [24] while enforcing the

abovementioned constraint equations. Subsequently, muscle recruitment was

performed to compute the muscle and joint reaction forces, including the unilateral

reaction forces of the TMJ, using a polynomial recruitment criterion with the muscle

activities cubed [25]. For later comparison with the FDK model, the medial/lateral

reaction force was split into two, such that, when it was pointing to the right, it was

referred to the right TMJ and vice-versa to the left TMJ.

FDK TMJ model

In the second model, the TMJ was modeled with three FDK DOFs. These were

defined as the movements in the normal directions of the rotated planes used to define

the POP constraints and the medial/lateral movement. To restrict and stabilize the now

free motions, models of the contacting surfaces of the TMJ and the temporomandibular

ligaments were introduced.

Each temporomandibular ligament was modeled as three nonlinear line

elements, which include a slack region, a polynomial toe region at low strain and a linear

region for high strain [27]:

$$f_l = \begin{cases} \dfrac{k\varepsilon^2}{4\varepsilon_l} & 0 \le \varepsilon \le 2\varepsilon_l \\ k(\varepsilon - \varepsilon_l) & \varepsilon \ge 2\varepsilon_l \\ 0 & \varepsilon < 0, \end{cases} \tag{15}$$

where f_l is the tensile force in the ligament, k is the ligament stiffness (in Newton per

unit strain), ε is the strain and ε_l is the linear strain limit, which was set to 0.03 [28].

The strain was computed based on the ligament length and slack length. Since the

19

subject-specific stiffness and slack length values of the ligaments were not known for the subject, a parameter study was performed as will be explained later.

The contacts between the skull and mandible at the TMJ were modeled with an elastic foundation contact model using the triangulated surface models of the bone geometries provided as STL files. To improve computation efficiency, the STL files only included the areas around the TMJs. To account for the missing soft tissue within the joints in the CT scans, the condyle surfaces were offset by 1 mm. The contact model computed the forces based on an approximation of the overlapping volume between the two STL surfaces and a linear contact law. This approximation uses the penetration depth, d_i, of the ith vertex of one triangle-mesh into the closest point on the opponent surface. The volume, v_i, of the ith triangular prism of height d_i and cross-sectional area, a_i, was computed as $v_i = a_i d_i$. The magnitude of the contact force of the ith element was computed by assuming a linear relationship between the penetration volume and the force magnitude, $f_i = pv_i$, with a so-called pressure modulus, p, as the coefficient. The pressure modulus was set to 10 GNm^{-3}. In this study, the pressure modulus is a non-physical quantity estimated to ensure that the penetration into the contact surfaces remains small and on the same order of magnitude as the kinematic tolerance.

With eight measured markers on the brace, a kinematically over-determinate system is obtained and the FDK analysis approach with over-determinate kinematics was therefore employed to compute the muscle, ligament and contact forces. Similar to the

POP model, a polynomial recruitment criterion with the muscle activities cubed was applied.

Parameter study

Since the specific TMJ ligament stiffness and slack length properties are not available for the test subject, a parameter study was conducted. Similarly to Chen et al. [29], the stiffness of the TMJ was initially assumed to be 272.4 Nm^{-1} and equally divided between each of the three TMJ ligament elements on the left and right side. As this value is uncertain, a parameter study was conducted in which the ligament stiffness was systematically set to 136.2 Nm^{-1}, 272.4 Nm^{-1} and 544.8 Nm^{-1}. The strain in the ligament was described by introducing a reference length, l_r, and a reference strain, ε_r:

$$\varepsilon = \frac{l - l_0}{l_0}$$
$$l_0 = \frac{l_r}{\varepsilon_r + 1},$$
(16)

where l_0 is the slack length. The length between origin and insertion of the ligament branches in the CT scan position was used as the ligament reference lengths.

For each of the three stiffness values, the reference strain was systematically varied from -0.04 to 0.04 in steps of 0.02 for all branches of the ligaments. This led to a total of 15 combinations of stiffness and reference strains.

Model evaluation

Differences between measured and estimated secondary joint kinematics and between FDK-predicted and POP-predicted TMJ reaction forces were quantified using Root-Mean-Square-Deviation (RMSD), squared Pearson's correlation coefficient (r^2) and the Sprague and Geer's metrics of differences in magnitude (M) and phase (P) [30]. For these comparisons, we used the FDK model with TMJ ligament stiffness of 272.4 Nm^{-1} and a reference strain of 0.0.

RESULTS

The results for the predicted and measured TMJ kinematics and forces are depicted in Figs. 5-7 and quantified in Tables 2 and 3.

The POP model generally predicted the AP and SI kinematics on both sides better than the FDK model with r^2 values between 0.98 and 1.00 on average and an RMSD of at most 0.57 mm. This excellent prediction of the kinematics was also observed in the magnitude error, which was at most 8 % on average. However, although the RMSD in the ML directions were generally below 0.75 mm, the r^2 was generally low. This is likely caused by the model, which does not allow ML movement, and the low range-of-motion of this DOF that leads to a low signal-to-noise ratio.

The FDK model generally produced good estimates for the kinematics for the AP and SI DOFs with the exception of the right SI for the chewing movement, which had a lower r^2. Although the RMSD was slightly higher for the FDK model compared to the POP model

for the ML direction, the r^2 was generally higher, which indicates that the curve shapes are better captured by the FDK model.

While the TMJ kinematics generally compared well between the two TMJ model types and the measured kinematics, the estimated TMJ reaction forces showed substantial differences. For the SI direction, the POP model demonstrated a lower force than the FDK model for all movements as observed by the negative magnitude differences in Table 2. The smallest difference of -0.20 in the SI force magnitude error was observed for the right TMJ during the chewing movement and the highest during the protrusion movement of -0.51. A force difference of more than 100% was found in the AP direction of the right TMJ during the open-close movement.

The results of the parameter study on the ligament properties demonstrated that the associated variation of the results is on the same order of magnitude as the five repetitions of the trials and must be considered less sensitive parameters in this model.

DISCUSSION

The first aim of this study was to provide the theoretical foundation of the FDK methodology and extend the original method with the capability of handling over-determinate kinematic information. To this end, we developed a general analysis framework to compute muscle forces, joint reaction forces and secondary joint kinematics that can be applied to any musculoskeletal model with any desired joint model as long as the bones can be considered rigid and the forces occurring within the joint can be described in terms of the position, velocity and acceleration coordinates.

The second aim was to apply the extended FDK method to the analysis of a subject-specific mandible model to estimate TMJ kinematics and reaction forces. The predicted secondary joint kinematics were compared to measured kinematics obtained with a custom-built brace and the kinematics obtained with a POP TMJ model. Finally, we compared the estimated TMJ forces between the two models. We found a good agreement between the secondary joint kinematics computed with FDK and the measured joint kinematics in terms of RMSD. For this particular subject, the POP model produced better estimates of the TMJ kinematics than the FDK model. However, both models showed only small error magnitudes.

In terms of the estimated TMJ reaction forces, substantial differences were observed between the two models but as direct measurements of the reaction forces are not available, it is not possible to conclude which of the two predictions is more accurate. For the POP model, the orientation of the reaction force is prescribed by the orientation of the plane except in the ML direction which is split between the two condyles depending on the sign of the ML force. Since the orientation of the plane is an input to the model, the resultant force depends on the accuracy of the orientation of the plane and, not least, on how accurately the assumption of a plane represents the underlying geometry. On the contrary, with the FDK approach, the joint can be modeled directly based on the subject-specific information that can be acquired from medical images and does not require the kinematics and force-directions to be prescribed. This has several advantages when applying this type of model to the analysis of pathological cases or the development of joint replacements, where the resulting kinematics may

not be known a priori. However, for the example model used in this study, the results indicate that using only the bone geometry with a 1 mm offset is insufficient to fully capture the detailed mechanics of the TMJ where especially the movements of the articular disc has been omitted in the model. A natural next step with the FDK TMJ model would be to include a more detailed model of the articular disc, TMJ ligament and capsule. Especially the poor estimation results for the SI kinematics of the right TMJ during the chewing movement indicates that the FDK TMJ model requires improvements of the TMJ representation. Since the movement in this direction is primarily controlled by the contact between the condyle and the mandibular fossa, this increased error compared to other DOFs suggests that a better model of the articular disc would lead to improvement. Such an articular disc could be introduced as a separate body and its movements controlled with FDK DOFs.

Although it is generally difficult to compare to previous simulation studies due to differences in modeling methodologies and reported outcomes, comparable studies of unloaded chewing and open-close movements are available. Hannam et al. [31] presented simulation results for unloaded chewing and both the mandible kinematics and the superior/inferior forces are qualitatively comparable to our FDK model. On the contralateral side (right in our model), Hannam et al. [31] reported a double hump in the superior/inferior force, which is also qualitatively present for the FDK model although the hump is larger in our simulations. The POP model showed a more symmetrical superior/inferior force on both sides and it does not present a double hump in the contralateral side. Qualitatively, the anterior/posterior and medial/lateral

force of the model of Hannam et al. [31] shows the same tendencies in terms of timing as the POP model. This is likely caused by similarities in the models although the model of Hannam et al. has taken the s-shape of the TMJ into account. Differences in the predictions of the model of Hannam et al. and the POP model on the one side and the predictions of the FDK model on the other side are seen particularly in the medial/lateral direction. This is likely because the FDK model takes into account the curvature of the TMJ in this direction. During a simulated open and close cycle, Tuijt [32] reported larger forces in the TMJ during the opening phase compared to the closing phase. However, we did not find such a clear pattern with our models. Over the five repeated trials, the left TMJ forces generally showed a pattern of the force being larger during the closing phase compared to the opening phase except for a couple of the trials where the forces were similar in the two phases for both model types. For the right TMJ forces, both models estimated almost similar forces during opening and closing except in a few trials where the opening force was larger than the closing force. There were, however, large differences in the forces between the different repetitions in the trials, which is also indicated by the large variations in the forces seen in Fig. 6. The reason for these differences in predicted forces is unknown but could be related to differences in the simulated subject or the modeling approach and comparison of the two simulation techniques on the same experimental data would be required to deduce the cause of the differences.

In recent years, there has been an increased focus on the development of methods that allow detailed joint models. Largely, this has been caused by the Grand

Challenge Competition to Predict In Vivo Knee Loads [33] and focus on the knee joint. Compared to other recently developed simulation methods that can include detailed joint descriptions such as Thelen et al. [14] and Guess et al. [34], the FDK approach offers some advantages. Both the methods of Thelen et al. [14] and Guess et al. [34] contain non-physiological controller parameters that must be chosen whereas the FDK approach as such does not contain such parameters. These controllers introduce non-physiological dynamics into the predictions and their impact depends on manually tuned parameters. Although the pressure modulus in the mandible was chosen as a non-physiological parameter, its impact on the simulations is likely minor due to the small penetrations obtained. The parameter could be estimated based on material properties, but this would likely lead to stiff contact models that are potentially difficult to solve numerically. Theoretically, there is no limitation to how the contact forces and models of the soft tissues can be defined. In this particular study of the mandible, we applied elastic foundation theory to compute the contact force based on STL files. However, the contact force could also have been described using Discrete-element Analysis or even Finite-element analysis. The considerations of which approach to apply are the associated computational cost, the required accuracy of the solutions to the various nonlinear equations and the desired output variables. In our case, the motivation for introducing a contact force description and a nonlinear description of the ligaments was to improve the simulated movements in non-conforming joints as these affect the moment arms of the muscles and external forces, which subsequently affect the predicted forces. The aim was not to accurately predict the contact pressures as this

can be accomplished more accurately in a detailed joint model specifically setup for this purpose and with the forces estimated by the musculoskeletal model as boundary conditions. Therefore, we opted to apply a non-physiological parameter for the pressure modulus in the TMJ model as this resulted in penetrations of the surfaces comparable to the applied kinematic tolerance applied when solving the nonlinear least-square optimization problem in Eq. (4). To compute the movements of the FDK DOFs that resulted in the FDK residual forces to be smaller than a specified tolerance, we applied a nonlinear equation solver based on a Newton-Raphson scheme augmented with a golden section line search. As part of this process, we approximated the Jacobian matrix of the FDK residual forces with respect to the FDK DOFs using a central finite difference method. This was done to ease the implementation of the FDK solution scheme but at the expense of increased computation time compared to an implementation with an analytical Jacobian. Despite this, the mandible model simulations each only took a few minutes to complete. In the interest of speed, accuracy and robustness, implementation of analytical Jacobians should be explored in the future. The main difficulties associated with this derivation is to determine the derivatives of the muscle recruitment, the nonlinear force-displacement relationships applied for the contact forces and soft tissues, the approximated velocity and acceleration analysis, and not least wrapping muscles.

As mentioned in the introduction, the FDK methodology has already been applied to several other joints of the body and, in particular, for validation studies of the predicted contact forces in the knee compared to those measured with an instrumented

prosthesis from the Grand Challenge data set [20,35], and showed good results.

Additionally, Marra et al. [20] compared the predicted joint kinematics against single

plane fluoroscopy during an unloaded leg swing and found a very good match between

the model and the experiment. However, this only investigated the sagittal plane

kinematics and not the secondary joint kinematics, as these were not measured.

Unfortunately, no full data set exist with both full lower limb medical imaging, measured

ground reaction forces and bi-planar fluoroscopy or bone pins for validation of the

secondary joint kinematics although this would be highly valuable for model validation

and should be explored in the future. As we do not have access to bi-planar fluoroscopy,

we opted for developing a model of the mandible as its movements can be measured

non-invasively and, hereby, provides an ideal option for direct model validation as

shown in this study. Additionally, the mandible model has several potential applications

such as planning of orthodontic surgery.

The present study contains some limitations that are worth discussing. First, the

FDK method assumes that the dynamics occurring in the FDK DOFs are negligible. From

our experiences with knees [20] and mandible models, this is a reasonable assumption,

which indicates that these joints experience a significant amount of damping. This is also

indicated by the measured and estimated TMJ kinematics depicted in Figs. 5-8, where

the measured TMJ kinematics does not show dynamic components that were not

estimated with the FDK model. Second, we have only validated the model predictions

for one subject and it is, therefore, unknown whether the results obtained when

comparing to the measured TMJ kinematics represent an outlier or not. To fully

understand the accuracy of the FDK TMJ model with the current level of detail, more subjects must be analyzed. Also, to estimate the TMJ kinematics based on the marker trajectories of the brace, the registration of the brace to the cone beam scan relied on the identification of the marker landmarks on the surface of the segmented cone beam scan. Unfortunately, this approach introduces a bias of unknown magnitude although we tried to minimize this by ensuring that it was the same examiner that placed the markers on the subject and model. In a future study, this bias could be reduced by either obtaining the cone beam scan while the subject is wearing the brace or by instrumenting the subject with markers that are visible in the scan. Third, no attempt was made to adjust the TMJ ligament properties of the subject. However, our sensitivity analysis of the stiffness and reference strain shows that the variation in results caused by these parameters has the same order of magnitude as the five repetitions of the trials performed by the subject and, therefore, only have a small impact on the predictions. Finally, a ML constraint in the POP model was introduced similar to de Zee et al. [10] but, as this constraint forces the mandible to pivot around a point on the AP axis, it will affect the predicted kinematics in the cases where the teeth move to the left or right as the rotation will, in these cases, occur around the respective condyle and not mid-way between the condyles. This may have affected the POP model estimations during the chewing movements but as the FDK model does not include such a constraint, it will not be affected by this limitation.

In conclusion, we presented the mechanical and mathematical foundation of the novel FDK method and demonstrated how it can be used to develop a subject-specific

30

mandible model. Since the FDK approach allows detailed joint models described with force elements, it opens up new opportunities for modeling and studying the detailed mechanics of joints for which an explicit kinematic description is not easy to obtain or for non-conforming joints where the joint elasticity plays a significant role.

ACKNOWLEDGMENT

FUNDING

REFERENCES

[1] Mellon SJ, Grammatopoulos G, Andersen MS, Pegg EC, Pandit HG, Murray DW, et al. Individual motion patterns during gait and sit-to-stand contribute to edge-loading risk in metal-on-metal hip resurfacing. Proc Inst Mech Eng H 2013 Jul;227(7):799-810.

[2] Rasmussen J, Tørholm S, de Zee M. Computational analysis of the influence of seat pan inclination and friction on muscle activity and spinal joint forces. Int J Ind Ergonomics 2009 1;39(1):52-57.

[3] Mirakhorlo M, Azghani MR, Kahrizi S. Validation of a musculoskeletal model of lifting and its application for biomechanical evaluation of lifting techniques. J Res Health Sci 2014;14(1):23-28.

[4] Crowninshield RD. Use of Optimization Techniques to Predict Muscle Forces. J Biomech Eng 1978 May 1978;100(2):88-92.

[5] Rasmussen J, Damsgaard M, Voigt M. Muscle recruitment by the min/max criterion - A comparative numerical study. J Biomech 2001;34(3):409-415.

[6] Thelen DG, Anderson FC. Using computed muscle control to generate forward dynamic simulations of human walking from experimental data. J Biomech 2006;39(6):1107-1115.

[7] Buchanan TS, Lloyd DG, Manal K, Besier TF. Neuromusculoskeletal modeling: Estimation of muscle forces and joint moments and movements from measurements of neural command. Journal of applied biomechanics 2004;20(4):367.

[8] Anderson FC, Pandy MG. Dynamic optimization of human walking. J Biomech Eng 2001;123(5):381-390.

[9] Erdemir A, McLean S, Herzog W, van den Bogert AJ. Model-based estimation of muscle forces exerted during movements. Clin Biomech 2007;22(2):131-154.

[10] de Zee M, Dalstra M, Cattaneo PM, Rasmussen J, Svensson P, Melsen B. Validation of a musculo-skeletal model of the mandible and its application to mandibular distraction osteogenesis. J Biomech 2007;40(6):1192-1201.

[11] de Zee M, Hansen L, Wong C, Rasmussen J, Simonsen EB. A Generic Detailed Rigid-body Lumbar Spine Model. J Biomech 2007;40(6):1219-1227.

[12] Klein Horsman MD, Koopman HFJM, van der Helm FCT, Prosé LP, Veeger HEJ. Morphological muscle and joint parameters for musculoskeletal modelling of the lower extremity. Clin Biomech 2007 2;22(2):239-247.

[13] Benoit DL, Ramsey DK, Lamontagne M, Xu L, Wretenberg P, Renström P. Effect of skin movement artifact on knee kinematics during gait and cutting motions measured in vivo. Gait Posture 2006 10;24(2):152-164.

[14] Thelen DG, Choi KW, Schmitz AM. Co-Simulation of Neuromuscular Dynamics and Knee Mechanics during Human Walking. Journal of Biomechanical Engineering 2013;In press:doi:10.1115/1.4026358.

[15] Halloran JP, Ackermann M, Erdemir A, van den Bogert AJ. Concurrent musculoskeletal dynamics and finite element analysis predicts altered gait patterns to reduce foot tissue loading. J Biomech 2010 Oct 19;43(14):2810-2815.

[16] Lin Y-, Walter JP, Banks SA, Pandy MG, Fregly BJ. Simultaneous prediction of muscle and contact forces in the knee during gait. J Biomech 2010;43(5):945-952.

[17] Praagman M, Chadwick EKJ, Van Der Helm FCT, Veeger HEJ. The relationship between two different mechanical cost functions and muscle oxygen consumption. J Biomech 2006;39(4):758-765.

[18] Boyd S, Vandenberghe L. **Convex Optimization**. : Cambridge University Press; 2004.

[19] Andersen MS, Damsgaard M, Rasmussen J. A novel musculoskeletal modelling approach for non-conforming joints. In Proceedings of the 13th Biennial International Symposium on Computer Simulation in Biomechanics, Leuven, Belgium 2011.

[20] Marra MA, Vanheule V, Fluit R, Koopman BHFJM, Rasmussen J, Verdonschot N, et al. A Subject-Specific Musculoskeletal Modeling Framework to Predict In Vivo Mechanics of Total Knee Arthroplasty. J Biomech Eng 2015 February 1;137(2):020904-020904.

[21] Zhang X, Chen Z, Wang L, Yang W, Li D, Jin Z. Prediction of hip joint load and translation using musculoskeletal modelling with force-dependent kinematics and experimental validation. Proceedings of the Institution of Mechanical Engineers, Part H: Journal of Engineering in Medicine 2015 July 01;229(7):477-490.

[22] Sins L, Tétreault P, Hagemeister N, Nuño N. Adaptation of the AnyBody™ Musculoskeletal Shoulder Model to the Nonconforming Total Shoulder Arthroplasty Context. Journal of Biomechanical Engineering 2015 September 2;137(10):101006-101006.

[23] Ignasiak D, Dendorfer S, Ferguson SJ. Thoracolumbar spine model with articulated ribcage for the prediction of dynamic spinal loading. J Biomech 2015;doi:10.1016/j.jbiomech.2015.10.010 (In press).

[24] Andersen MS, Damsgaard M, Rasmussen J. Kinematic analysis of over-determinate biomechanical systems. Comput Methods Biomech Biomed Eng 2009;12(4):371-384.

[25] Damsgaard M, Rasmussen J, Christensen ST, Surma E, de Zee M. Analysis of musculoskeletal systems in the AnyBody Modeling System. Simul Model Pract Theory 2006;14(8):1100-1111.

[26] Koolstra JH, van Eijden TMGJ. Combined finite-element and rigid-body analysis of human jaw joint dynamics. J Biomech 2005 12;38(12):2431-2439.

[27] Blankevoort L, Huiskes R. Ligament-bone interaction in a three-dimensional model of the knee. J Biomech Eng 1991 Aug;113(3):263-269.

[28] Butler DL, Kay MD, Stouffer DC. Comparison of material properties in fascicle-bone units from human patellar tendon and knee ligaments. J Biomech 1986;19(6):425-432.

[29] Chen J, Akyuz U, Xu L, Pidaparti RMV. Stress analysis of the human temporomandibular joint. Med Eng Phys 1998 10;20(8):565-572.

[30] Schwer LE. Validation metrics for response histories: perspectives and case studies. Engineering with Computers 2007;23(4):295-309.

[31] Hannam AG, Stavness I, Lloyd JE, Fels S. A dynamic model of jaw and hyoid biomechanics during chewing. J Biomech 2008;41(5):1069-1076.

[32] Tuijt M, Koolstra JH, Lobbezoo F, Naeije M. Differences in loading of the temporomandibular joint during opening and closing of the jaw. J Biomech 2010 4/19;43(6):1048-1054.

[33] Fregly BJ, Besier TF, Lloyd DG, Delp SL, Banks SA, Pandy MG, et al. Grand challenge competition to predict in vivo knee loads. Journal of Orthopaedic Research 2012;30(4):503-513.

[34] Guess TM, Stylianou AP, Kia M. Concurrent Prediction of Muscle and Tibiofemoral Contact Forces During Treadmill Gait. Journal of Biomechanical Engineering 2014 February 5;136(2):021032-021032.

[35] Chen Z, Zhang Z, Wang L, Li D, Zhang Y, Jin Z. Evaluation of a subject-specific musculoskeletal modelling framework for load prediction in total knee arthroplasty. Med Eng Phys 2016 8;38(8):708-716.

Figure Captions List

Fig. 1   The FDK analysis framework. The block on the left illustrates the nonlinear

                equation solver based on a Newton-Raphson scheme augmented with a

                golden section line search. Throughout the execution of this solver, the

inverse dynamic analysis model is executed with the FDK DOFs, $\boldsymbol{\alpha}^{(\mathrm{FDK})}$, as input from which the FDK residual forces, $\mathbf{f}^{(\mathrm{FDK})}$, are computed. In the figure, the kinematic analysis is illustrated by the equations solved at position level but the equations subsequently solved to compute the velocities and accelerations are not shown in the figure. These can be seen in Eqs. (2) and (3) in the case of determinate kinematics and Eqs. (9) and (10) in case of over-determinate kinematics. For a description of the terms, please see the method section and the nomenclature list.

Fig. 2   (a) and (b) show the subject sitting in the reference position while wearing the brace and with the skin markers attached. The red circles indicate areas where skin markers were attached but later excluded due to difficulties in accurately defining their location on the surface of the CT scan. (c) Shows the laser scanned brace components registered to the CT scan. (d) and (e) show the musculoskeletal model and the defined anatomical reference frame. (f) Shows the subject-specific braces

Fig. 3   Illustration of the POP model without muscles. (a) shows a right side view of the model with the plane that the most superior point of the condyle was constrained to stay on. (b) is a zoom of the TJM with the constraint of the most superior point of the condyle (shown as a green dot) is restricted to only slide and rotate in that plane. Note that the constraint shown only apply in the viewing plane. The same constraint is applied on the left hand

side. (c) Shows a front view of the model with the planes of the left and right TMJs included. (d) Shows a top view of the mandible. The skull anatomical reference frame is indicated in black and the origin of the mandible anatomical reference frame is indicated as a green dot. The origin of the mandible anatomical frame is constrained such that it cannot move medial or lateral relative to the skull anatomical reference.

Fig 4   Illustration of the FDK model without muscles. (a) shows a right side view of the model and (b) a zoom of the TMJ. The three white lines illustrate the elements of the TMJ ligament and the small black arrows illustrate the contact forces for each triangle in the STL files. (c) and (d) illustrate the contact force of the right TMJ applied by the skull onto the mandible. Note that the skull and mandible were positioned with excessive penetration of the contacting surfaces into each other to clearly illustrate the contact forces.

Fig. 5   Simulation results for the chewing task. The two top rows show a comparison of the TMJ kinematics measured with the brace (red) and predicted with the POP model (green) and the FDK model (blue). The two bottom rows show the estimated TMJ forces with the POP model (green) and FDK model (blue). The grey area shows the results of the parameter study. The shaded areas indicate ± 1 standard deviation. Note that the grey areas largely overlap with the other areas.

Fig. 6   Simulation results for the Open-close task. The two top rows show a comparison of the TMJ kinematics measured with the brace (red) and predicted with the POP model (green) and the FDK model (blue). The two bottom rows show the estimated TMJ forces with the POP model (green) and FDK model (blue). The grey area shows the results of the parameter study. The shaded areas indicate ± 1 standard deviation. Note that the grey areas largely overlap with the other areas.

Fig. 7   Simulation results for the protrusion task. The two top rows show a comparison of the TMJ kinematics measured with the brace (red) and predicted with the POP model (green) and the FDK model (blue). The two bottom rows show the estimated TMJ forces with the POP model (green) and FDK model (blue). The grey area shows the results of the parameter study. The shaded areas indicate ± 1 standard deviation. Note that the grey areas largely overlap with the other areas.

Table Caption List

Table 1   Comparison of the predicted left and right TMJ kinematics against the joint kinematics measured with the custom brace for the FDK TMJ model and the POP TMJ model. The differences are quantified using Root-Mean-Square-Deviation (RMSD), squared Pearson's correlation coefficient, r^2, and the Sprague and Geer's metrics of magnitude (M) and phase (P).

Table 2   Comparison of the left and right TMJ reaction forces predicted by the POP model against the FDK TMJ model. The differences are quantified using Root-Mean-Square-Deviation (RMSD), squared Pearson's correlation coefficient, r^2, and the Sprague and Geer's metrics of magnitude (M) and phase (P).
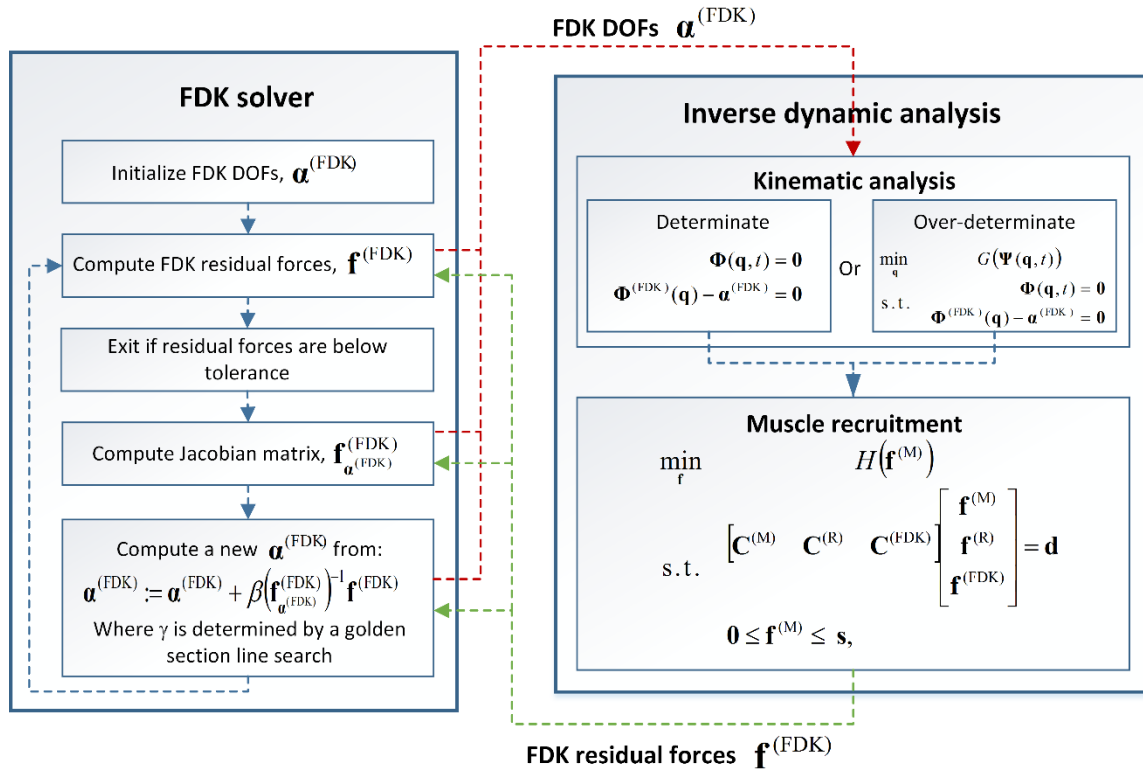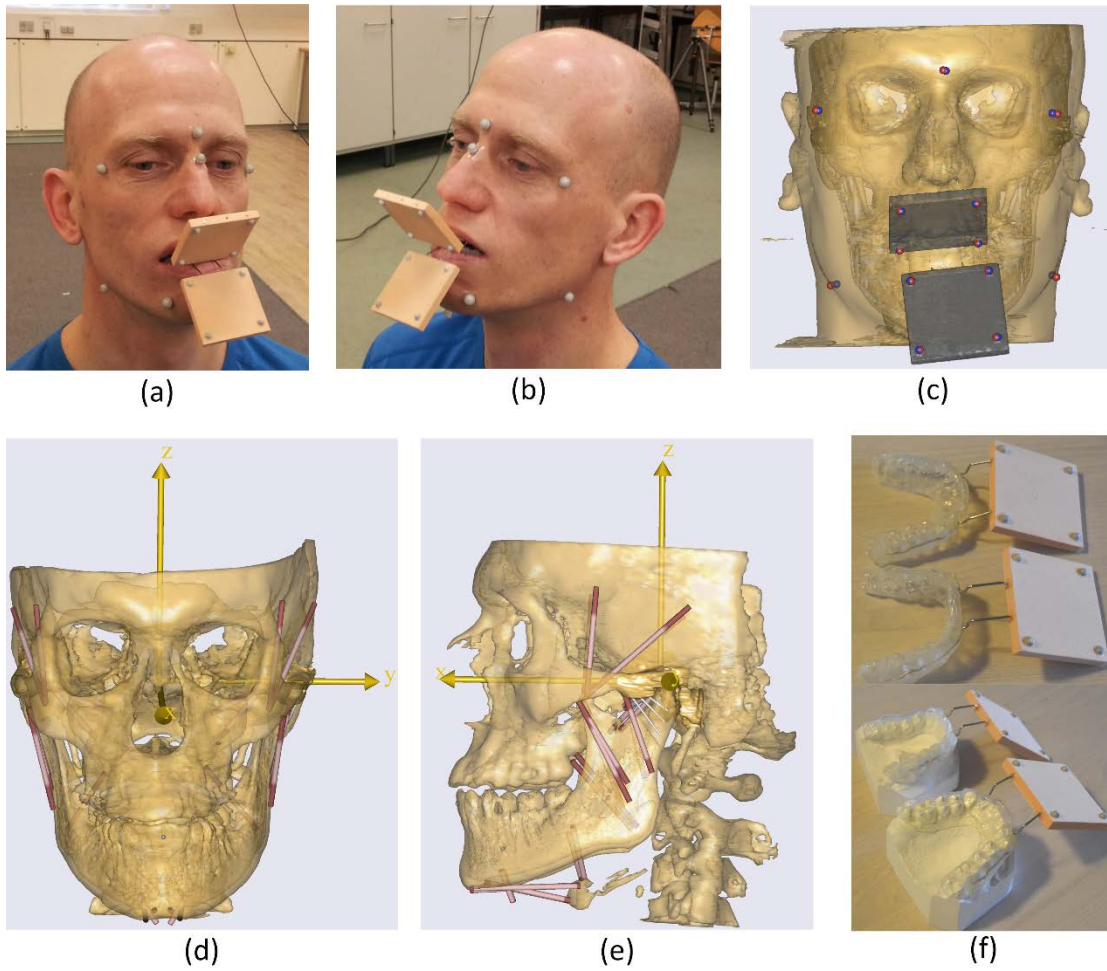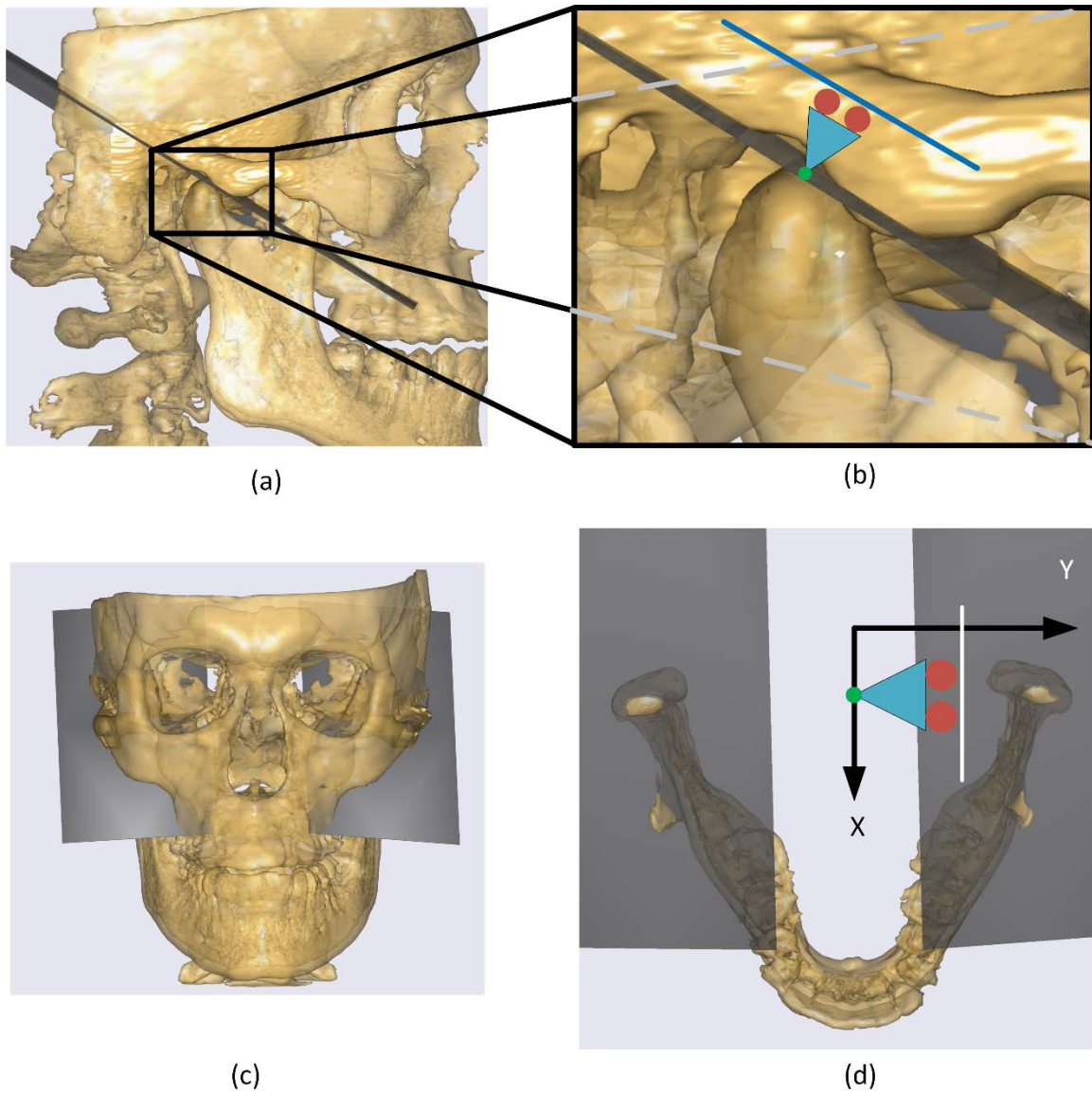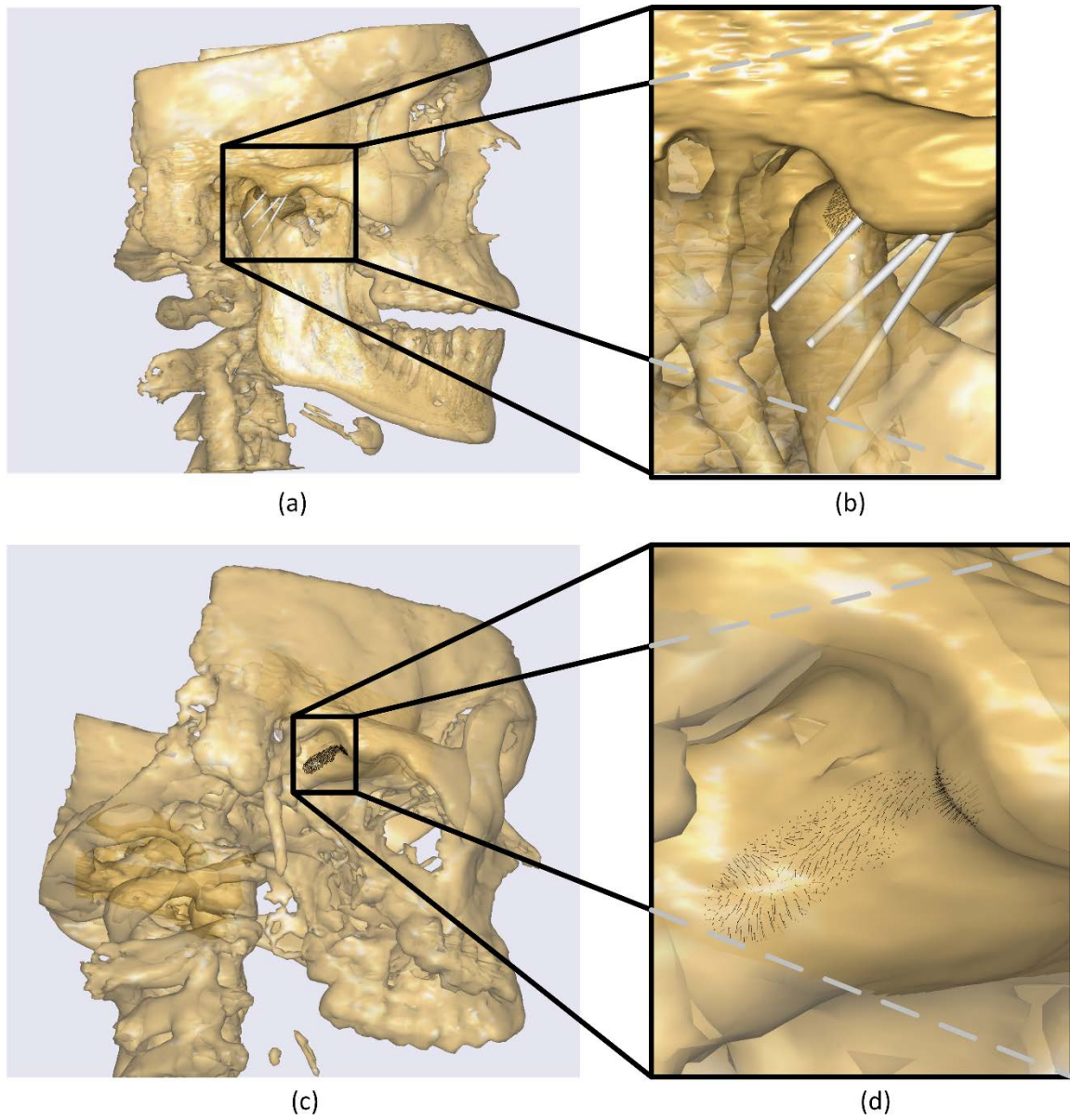
Fig 1

Fig 2

Fig 3

(a)

(b)

(c)

(d)

Fig 4

(a)

(b)

(c)

(d)

Fig 5
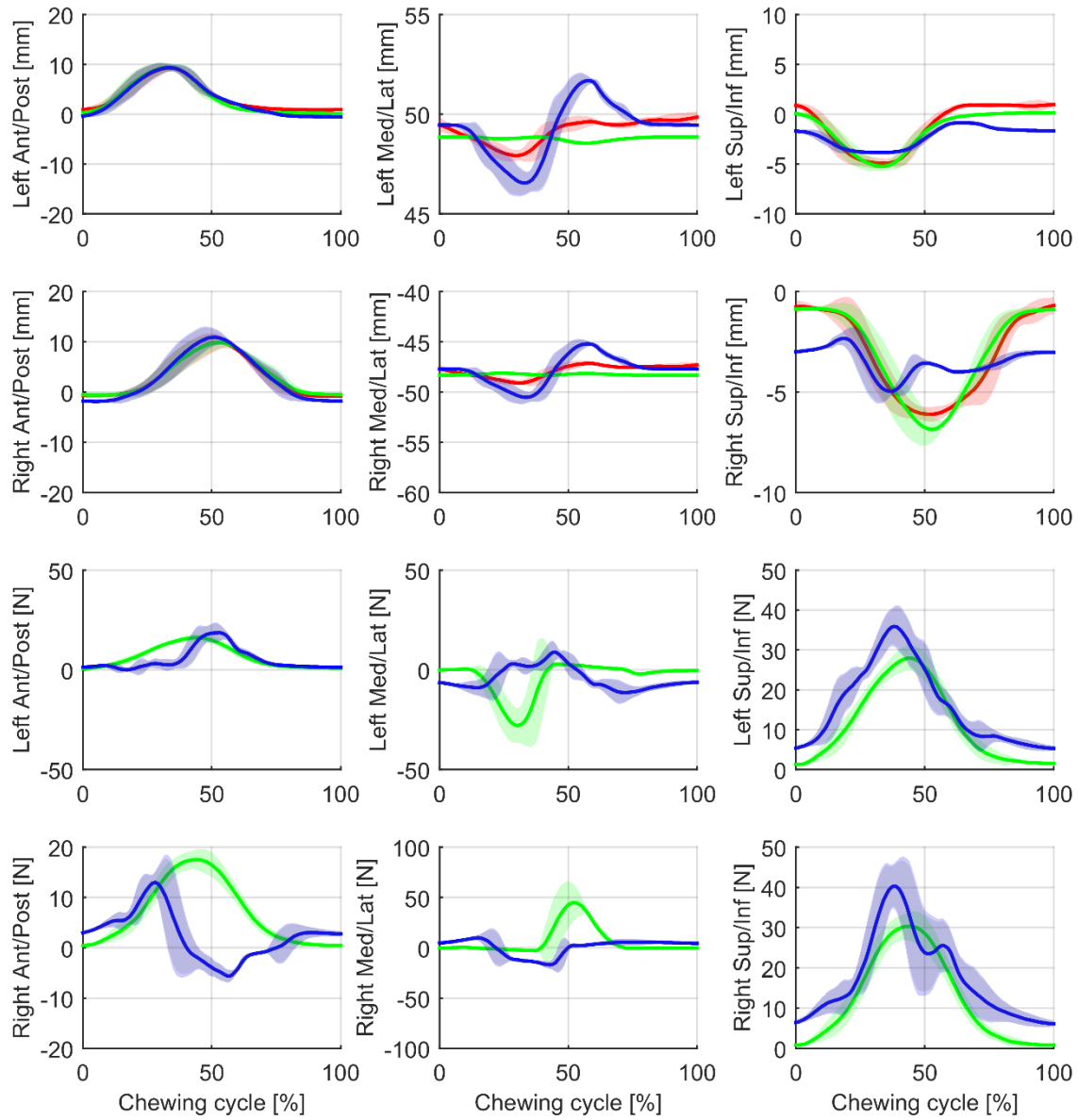
Fig 6
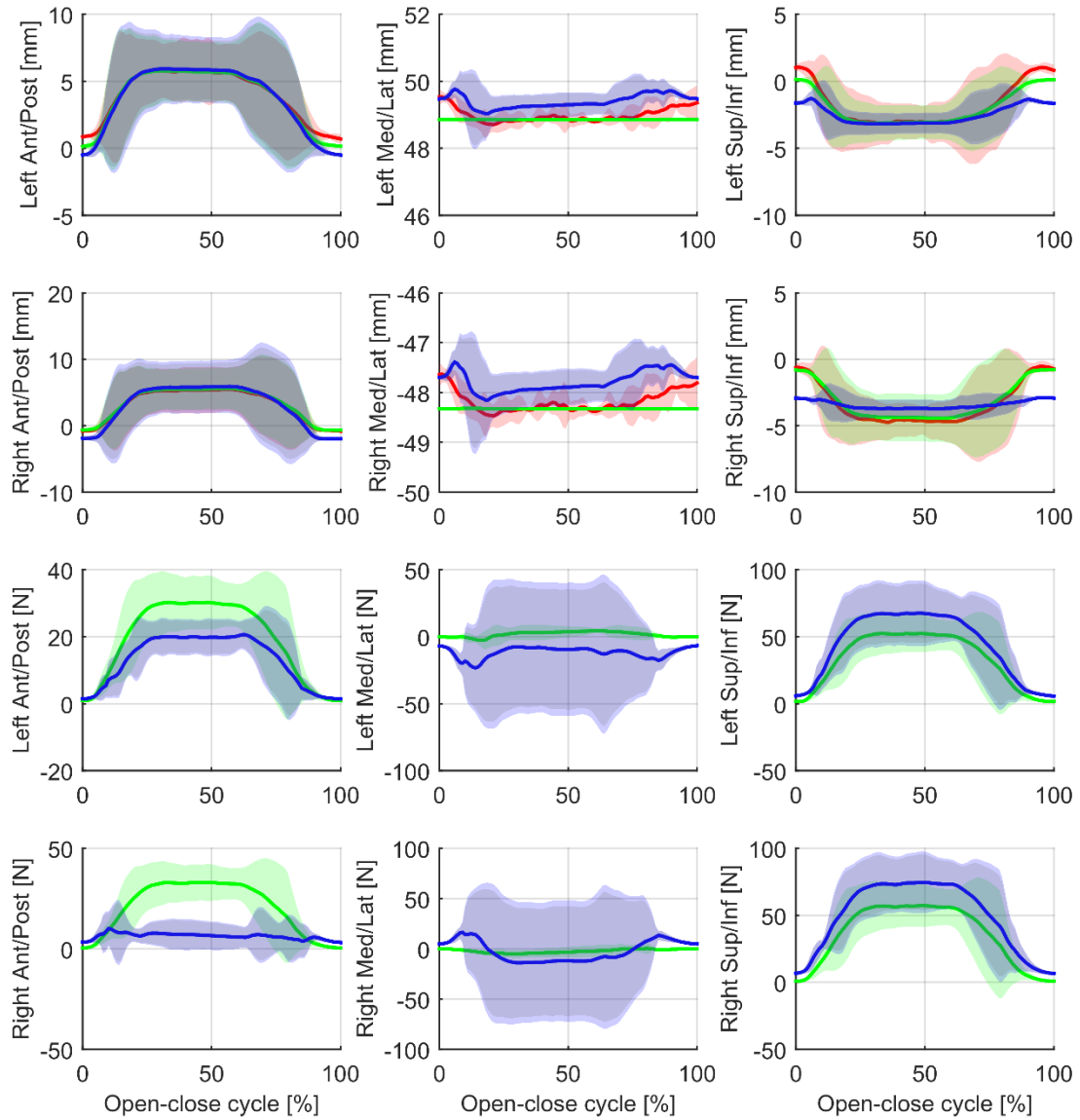
Fig 7
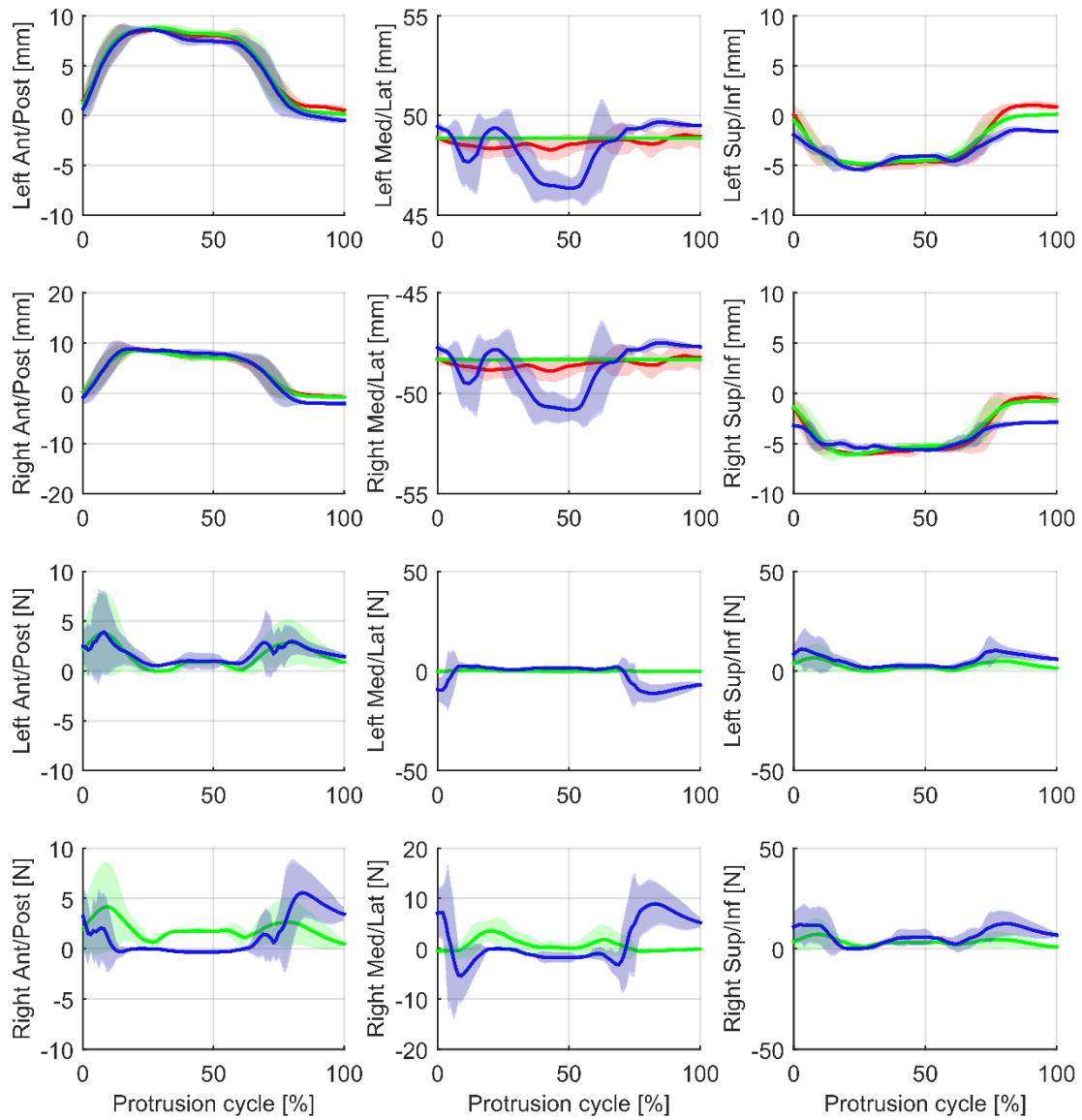
Table 1

Displacements	FDK TMJ model				POP TMJ model			
	RMSD[a]	r^2	M	P	RMSD[a]	r^2	M	P
Chewing								
Left AP	0.79±0.06	0.99±0.00	0.00±0.01	0.05±0.01	0.57±0.03	0.99±0.00	0.00±0.01	0.04±0.00
Left ML	0.98±0.07	0.70±0.13	0.00±0.00	0.01±0.00	0.74±0.04	0.03±0.03	-0.01±0.00	0.00±0.00
Left SI	1.70±0.09	0.93±0.01	-0.03±0.02	0.22±0.02	0.63±0.07	0.98±0.01	-0.03±0.02	0.08±0.01
Right AP	0.78±0.03	1.00±0.00	0.11±0.01	0.04±0.00	0.39±0.03	0.99±0.00	0.02±0.02	0.02±0.00
Right ML	0.95±0.07	0.79±0.11	0.00±0.00	0.01±0.00	0.75±0.04	0.12±0.06	0.01±0.00	0.00±0.00
Right SI	1.66±0.09	0.57±0.06	-0.06±0.03	0.14±0.01	0.48±0.10	0.96±0.02	-0.01±0.03	0.04±0.01
Open-close								
Left AP	0.61±0.04	0.99±0.01	0.00±0.05	0.04±0.02	0.35±0.04	0.99±0.00	-0.01±0.03	0.03±0.01
Left ML	0.48±0.10	0.30±0.13	0.01±0.00	0.00±0.01	0.27±0.03	0.21±0.05	0.00±0.00	0.00±0.00
Left SI	1.25±0.15	0.92±0.08	0.13±0.20	0.16±0.07	0.47±0.06	0.99±0.00	-0.02±0.03	0.07±0.04
Right AP	0.81±0.08	1.00±0.00	0.12±0.04	0.06±0.04	0.22±0.05	1.00±0.00	0.05±0.04	0.01±0.01
Right ML	0.47±0.10	0.32±0.12	-0.01±0.00	0.00±0.00	0.28±0.03	0.14±0.11	0.00±0.00	0.00±0.00
Right SI	1.41±0.06	0.85±0.12	-0.05±0.16	0.12±0.03	0.33±0.08	0.98±0.00	-0.08±0.05	0.02±0.00
Protrusion								
Left AP	0.59±0.07	0.99±0.00	-0.04±0.01	0.03±0.00	0.32±0.05	1.00±0.00	0.02±0.01	0.01±0.00
Left ML	1.16±0.14	0.18±0.11	0.00±0.00	0.01±0.00	0.37±0.12	0.05±0.08	0.01±0.00	0.00±0.00
Left SI	1.34±0.12	0.92±0.02	0.02±0.05	0.11±0.01	0.53±0.05	0.99±0.00	-0.04±0.02	0.04±0.01
Right AP	0.88±0.08	0.99±0.00	0.07±0.01	0.04±0.01	0.21±0.02	1.00±0.00	0.00±0.00	0.01±0.00
Right ML	1.16±0.14	0.18±0.12	0.00±0.00	0.01±0.00	0.37±0.11	0.06±0.10	-0.01±0.00	0.00±0.00
Right SI	1.25±0.10	0.91±0.02	0.00±0.03	0.09±0.01	0.40±0.07	0.98±0.00	-0.05±0.03	0.02±0.00

[a]RMSD is in unit of millimetres.

Table 2

TMJ reaction forces	FDK TMJ model vs POP TMJ model			
	RMSD[a]	r^2	M	P
Chewing				
Left AP	4.71±0.46	0.46±0.10	0.12±0.10	0.18±0.02
Left ML	12.5±1.44	0.14±0.09	0.35±0.21	0.51±0.01
Left SI	5.67±0.37	0.89±0.03	-0.21±0.04	0.08±0.01
Right AP	9.84±0.89	0.06±0.07	0.73±0.17	0.44±0.04
Right ML	17.88±2.87	0.00±0.00	0.92±0.43	0.50±0.02
Right SI	6.63±0.51	0.87±0.09	-0.20±0.04	0.09±0.02
Open-close				
Left AP	7.49±2.44	0.95±0.03	0.48±0.18	0.04±0.01
Left ML	18.69±12.25	0.37±0.32	-0.77±0.17	0.43±0.13
Left SI	12.17±4.05	0.99±0.01	-0.23±0.07	0.02±0.01
Right AP	19.29±5.42	0.09±0.13	3.34±2.66	0.19±0.03
Right ML	24.7±5.96	0.23±0.30	-0.86±0.08	0.53±0.26
Right SI	14.4±3.66	0.99±0.00	-0.25±0.07	0.03±0.01
Protrusion				
Left AP	0.75±0.13	0.64±0.21	-0.08±0.18	0.11±0.01
Left ML	5.46±1.01	0.37±0.32	-0.93±0.03	0.34±0.11
Left SI	3.25±0.25	0.73±0.19	-0.49±0.10	0.10±0.01
Right AP	2.37±0.37	0.14±0.21	-0.08±0.23	0.34±0.05
Right ML	5.14±1.14	0.14±0.08	-0.68±0.10	0.56±0.02
Right SI	4.68±0.67	0.38±0.26	-0.51±0.07	0.15±0.04

[a]RMSD is in unit of Newton.

Nomenclature

Variable	Dimensionality (rows x columns)	Description
n	Scalar	Number of rigid bodies
$n^{(M)}$	Scalar	Number of muscles
$n^{(R)}$	Scalar	Number of reaction forces
$n^{(FDK)}$	Scalar	Number of FDK DOFs
$n^{(\Phi)}$	Scalar	Number of hard constraints
$n^{(\Psi)}$	Scalar	Number of soft constraints
$n^{(\tilde{\Phi})}$	Scalar	Number of hard constraints remaining after those associated with pure movements have been omitted.
t	Scalar	Time
$\mathbf{r}_i$	3 x 1	Position vector of the center of mass of ith segment.
$\mathbf{p}_i$	4 x 1	Vector of Euler parameters for the ith segment
$\mathbf{q}_i$	7 x 1	Vector containing the position vector and Euler parameters of the ith segment
$\mathbf{q}$	$7n$ x 1	Vector containing the position vectors and Euler paremeter of all segments
$\dot{\mathbf{r}}_i$	3 x 1	Velocity vector of the center of mass of ith segment
$\boldsymbol{\omega}_i'$	3 x 1	Angular velocity vector of the ith rigid segment measured relative to its body-fixed reference frame
$\tilde{\boldsymbol{\omega}}_i'$	3 x 3	Skew-symmetric matrix associated with the angular velocity vector of the ith segment
$\mathbf{v}_i$	6 x 1	Vector containing the linear and angular velocity vectors for the ith segment
$\mathbf{v}$	$6n$ x 1	Vector containing the linear and angular velocity vectors of all segments
$\dot{\mathbf{v}}$	$6n$ x 1	Vector containing the linear and angular acceleration vectors of all segments
$\boldsymbol{\Phi}$	$n^{(\Phi)}$ x 1	Vector of hard constraint equations
$\boldsymbol{\Phi}^{(FDK)}$	$n^{(FDK)}$ x 1	Vector of FDK constraint equations
$\boldsymbol{\alpha}^{(FDK)}$	$n^{(FDK)}$ x 1	Vector of FDK position coordinates
$\dot{\boldsymbol{\alpha}}^{(FDK)}$	$n^{(FDK)}$ x 1	Vector of FDK velocity coordinates
$\ddot{\boldsymbol{\alpha}}^{(FDK)}$	$n^{(FDK)}$ x 1	Vector of FDK acceleration coordinates
$\hat{\mathbf{q}}$	$6n$ x 1	Vector of a virtual set of positions that correspond to $\mathbf{v}$
$\boldsymbol{\Phi}_{\hat{\mathbf{q}}}$	$n^{(\Phi)}$ x $6n$	Jacobian matrix of the hard constraint equations with respect to $\hat{\mathbf{q}}$
$\boldsymbol{\Phi}_{\hat{\mathbf{q}}}^{(FDK)}$	$n^{(FDK)}$ x $6n$	Jacobian matrix of the FDK constraint equations with respect $\mathbf{q}^*$

$\mathbf{\Phi}_t$	$n^{(\mathbf{\Phi})}$ x 1	Vector of the partial derivatives of the hard constraint equations with respect to time
$\mathbf{\gamma}$	$n^{(\mathbf{\Phi})}$ x 1	Vector of position- and velocity-dependent terms emerging from the differentiation of the hard constraint equations, $\mathbf{\Phi}$, with respect to time.
$\mathbf{\gamma}^{(\text{FDK})}$	$n^{(\text{FDK})}$ x 1	Vector of position- and velocity-dependent terms emerging from the differentiation of the function $\mathbf{\Phi}^{(\text{FDK})}$, with respect to time
$\mathbf{\Psi}$	$n^{(\mathbf{\Psi})}$ x 1	Vector of soft constraint equations
G	Scalar	Objective function of the soft constraint equations
$\mathbf{W}$	$n^{(\mathbf{\Psi})}$ x $n^{(\mathbf{\Psi})}$	Weight matrix applied in the objective function of a weighted least-square optimization problem for over-determinate kinematics
$\mathbf{\delta}$	$n^{(\mathbf{\Psi})}$ x 1	Vector of residuals on the soft constraint equations
$\dot{\mathbf{\delta}}_{\text{approx}}$	$n^{(\mathbf{\Psi})}$ x 1	Vector of approximated velocities of the residual vector $\mathbf{\delta}$
$\ddot{\mathbf{\delta}}_{\text{approx}}$	$n^{(\mathbf{\Psi})}$ x 1	Vector of approximated accelerations of the residual vector $\mathbf{\delta}$
Δt	Scalar	Time increment used in the approximate velocity and acceleration analysis
$\mathbf{\Psi}_{\hat{\mathbf{q}}}$	$n^{(\mathbf{\Psi})}$ x $6n$	Jacobian matrix of the soft constraint equations with respect to $\hat{\mathbf{q}}$
$\mathbf{\Psi}_t$	$n^{(\mathbf{\Psi})}$ x 1	Vector of the partial derivatives of the soft constraint equations with respect to time
$\mathbf{\gamma}^{(\Psi)}$	$n^{(\mathbf{\Psi})}$ x 1	Vector of position- and velocity-dependent terms emerging from the differentiation of the soft constraint equations, $\mathbf{\Psi}$, with respect to time
H	Scalar	Muscle recruitment objective function
$\mathbf{f}^{(\text{M})}$	$n^{(\text{M})}$ x 1	Muscle forces
$\mathbf{f}^{(\text{R})}$	$n^{(\text{R})}$ x 1	Reaction forces
$\mathbf{f}^{(\text{FDK})}$	$n^{(\text{FDK})}$ x 1	FDK residual forces
$\mathbf{C}_i^{(\text{M})}$	6 x $n^{(\text{M})}$	Coefficient matrix for the muscle forces on the ith segment
$\mathbf{C}_i^{(\text{R})}$	6 x $n^{(\text{R})}$	Coefficient matrix for the reaction forces on the ith segment
$\mathbf{C}_i^{(\text{FDK})}$	6 x $n^{(\text{FDK})}$	Coefficient matrix for the FDK residual forces on the ith segment
$\mathbf{C}^{(\text{M})}$	$6n$ x $n^{(\text{M})}$	Coefficient matrix for the muscle forces on all segments
$\mathbf{C}^{(\text{R})}$	$6n$ x $n^{(\text{R})}$	Coefficient matrix for the reaction forces on all segments

49

$\mathbf{C}^{(FDK)}$	$6n$ x $n^{(FDK)}$	Coefficient matrix for the FDK residual forces on all segments
$\mathbf{s}$	$n^{(M)}$ x 1	Vector of instantaneous muscle strengths
$\mathbf{I}$	3 x 3	Identity matrix
$\mathbf{J}'_i$	3 x 3	Mass moment of inertia tensor refering to the body-fixed reference frame of the ith segment
$\mathbf{g}_i^{(app)}$	6 x 1	Vector of applied loads on the ith segment
$\mathbf{d}_i$	6 x 1	Vector of applied loads minus the inertial and gyroscopic terms for the ith segment
$\mathbf{d}$	$6n$ x 1	Vector of applied loads minus the inertial and gyroscopic terms for all segments
${}^i l_{\hat{\mathbf{q}}}^{(oi)}$	1 x $6n$	The partial derivative of the origin to insertion length of the ith muscle with respect to $\hat{\mathbf{q}}$.
$\tilde{\mathbf{\Phi}}$	$n^{(\tilde{\Phi})}$ x 1	Subset of constraint equations from $\mathbf{\Phi}$ where constraints specifying pure movement have been omitted.
$\mathbf{f}_{\alpha^{(FDK)}}^{(FDK)}$	$n^{(FDK)}$ x $n^{(FDK)}$	Jacobian matrix of the FDK residual forces derived with respect to the FDK DOFs
β	Scalar	Step length applied in the FDK solver
f_l	Scalar	Magnitude of a ligament force
k	Scalar	Ligament stiffness
ε	Scalar	Ligament strain
ε_l	Scalar	Ligament linear strain limit
d_i	Scalar	Penetration depth of the ith vertex into the closest triangle on the opposite surface
a_i	Scalar	Area of the triangle closest to the ith vertex
v_i	Scalar	Penetration volume of the ith vertex
p	Scalar	Pressure modulus
f_i	Scalar	Contact force from the ith vertex
l	Scalar	Ligament length
l_0	Scalar	Ligament slack length
l_r	Scalar	Ligament reference length
ε_r	Scalar	Ligament reference strain